

Spin order and phase transitions in chains of polariton condensates

H. Ohadi,^{1,*} A. J. Ramsay,² H. Sigurdsson,³ Y. del Valle-Inclan Redondo,¹ S. I. Tsintzos,⁴ Z. Hatzopoulos,⁴
T. C. H. Liew,⁵ I. A. Shelykh,^{3,6} Y. G. Rubo,^{7,8} P. G. Savvidis,^{4,6,9} and J. J. Baumberg^{1,†}

¹*Department of Physics, Cavendish Laboratory, University of Cambridge, Cambridge CB3 0HE, United Kingdom*

²*Hitachi Cambridge Laboratory, Hitachi Europe Ltd., Cambridge CB3 0HE, UK*

³*Science Institute, University of Iceland, Dunhagi-3, IS-107 Reykjavik, Iceland*

⁴*FORTH, Institute of Electronic Structure and Laser, 71110 Heraklion, Crete, Greece*

⁵*School of Physical and Mathematical Sciences, Nanyang Technological University 637371, Singapore*

⁶*ITMO University, St. Petersburg 197101, Russia*

⁷*Instituto de Energías Renovables, Universidad Nacional Autónoma de México, Temixco, Morelos, 62580, Mexico*

⁸*Center for Theoretical Physics of Complex Systems,
Institute for Basic Science (IBS), Daejeon 34051, Republic of Korea*

⁹*Department of Materials Science and Technology,
University of Crete, 71003 Heraklion, Crete, Greece*

We demonstrate that multiply-coupled spinor polariton condensates can be optically tuned through a sequence of spin-ordered phases by changing the coupling strength between nearest neighbors. For closed 4-condensate chains these phases span from ferromagnetic (FM) to antiferromagnetic (AFM), separated by an unexpected crossover phase. This crossover phase is composed of alternating FM-AFM bonds. For larger 8 condensate chains, we show the critical role of spatial inhomogeneities and demonstrate a scheme to overcome them and prepare any desired spin state. Our observations thus demonstrate a fully controllable non-equilibrium spin lattice.

Spin models, such as the Ising model, have been very successful in describing a wide range of condensed matter phenomena [1]. In addition, these models can be mapped to real-world optimization problems [2, 3], for example in transport scheduling, artificial intelligence, and financial portfolio optimization [4, 5]. Consequently, there is a growing interest in building controlled spin lattices both to study computationally complex spin systems such as spin glasses [6], but also as a potential computing architecture [7, 8]. Several systems have been explored, including ultracold atoms [9], degenerate optical parametric oscillators [10, 11], electromechanical resonators [12], and CMOS transistors [4, 5, 13]. Recently, individual exciton-polariton (polariton) condensates [14–21] have been observed to spontaneously magnetize [22], and when two condensates are close together the spins can be controllably aligned (or anti-aligned) [23]. Using these building blocks, we now explore the scaling up to a large 1D system, constructing a non-equilibrium, driven-dissipative controlled spin-lattice of exciton-polariton condensates. New types of order can appear in larger lattices, while at the same time extra measures have to be taken to ensure scalability.

Here, we study the spin properties of a closed interacting chain of exciton-polariton condensates. When the pump laser is turned on, the system spontaneously condenses into a magnetically ordered state on picosecond timescales, and remains frozen in that state for many milliseconds. By optically tuning the Josephson coupling between the condensates, the system can be tuned from a ferromagnetic to anti-ferromagnetic phase, via a dis-

ordered crossover phase. Remarkably, in a system of 4 identical spin condensates, where there is no spatial disorder a paired spin state with alternating FM-AFM bonds is observed. Such a state cannot exist in a smaller system. Furthermore, despite the larger phase degree-of-freedom offered by the larger spin chain, from comparison to theory we conclude that the FM (AFM) bonds only adopt a phase-shift of 0 (π) respectively. This locking of the phase and spin effectively results in a binary spin system. As the system size is increased to longer condensate chains, spatial inhomogeneity in the microcavity becomes an issue. We demonstrate a strategy to engineer ferromagnetic, antiferromagnetic, or glassy states of longer spin chains by simultaneously tailoring each individual nearest neighbor (NN) coupling between sites. Our work introduces interacting trapped polariton condensates as a controllable system for studying complex non-linear spin models out of equilibrium.

Polaritons are mixed light-matter quasiparticles appearing due to the strong coupling of photons in a microcavity and excitons in a semiconductor quantum well [24]. Polaritons are driven-dissipative bosons which can condense into macroscopically coherent many-body states [14–17]. High optical accessibility, picosecond dynamics, large non-linearity [25] and other unique properties [26–32], with potential application in semiconductor chip devices [18, 19, 33–37] make them particularly attractive.

Our system is a GaAs quantum-well microcavity (see SI. 1) with an optically-induced two-dimensional square lattice potential where a magnetized polariton condensate (emitting almost fully-circularly polarized light) forms at each lattice site (Fig. 1a-c). We generate polaritons by the non-resonant optical excitation of the microcavity. Each non-resonantly pumped spot creates a

* ho278@cam.ac.uk

† jjb12@cam.ac.uk

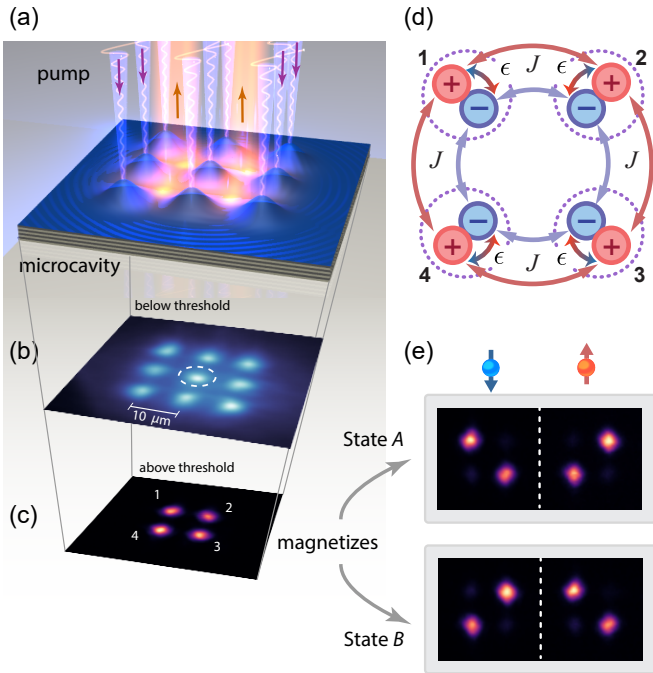


FIG. 1. (a) Lattice potential in the microcavity created by blueshifts at the pump beams (purple beams) forming magnetized condensates in the center of each site (yellow spots). (b) Below threshold PL showing the pump spots. Global NN barrier is tuned by modulating the intensity of the center spot (u_r , dashed circle). (c) Formation of condensates at the center of each of the 4 lattice sites above threshold. (d) Schematic of condensate spin chain comprised of two coupled Bose-Hubbard chains. Each condensate (indices 1–4) has two spin states (+ and –) which are coherently coupled by ϵ . Each is also coherently coupled to its same spin NN by Josephson coupling J . (e) Magnetization of condensate chain (expt) above the spin-bifurcation threshold (P_c), into an AFM state.

local reservoir of hot excitons which rapidly lose energy and flow out due to repulsion from hot excitons in the reservoir and repulsive self-interactions. Therefore, the optical excitation acts as both the gain and the trapping potential forming the lattice sites [38, 39]. Polaritons scatter into the ground state by stimulated scattering and final-state bosonic amplification [25]. Once the density at any site surpasses a threshold, a macroscopically coherent condensate forms inside each trap [30, 40].

The total spin of the polaritons is quantized along the structure growth axis, which corresponds to right- and left-circularly polarized photons emitted from the cavity. For pump powers exceeding a spin-bifurcation threshold, trapped polaritons can spontaneously magnetize by condensing into a single, randomly-chosen spin state. The spin-bifurcation process is driven by the dissipation rate difference (γ) and energy splitting of the horizontally and vertically polarized polaritons (ϵ), which determine the spin-bifurcation threshold [22]. We operate above this threshold, which means each condensate spontaneously

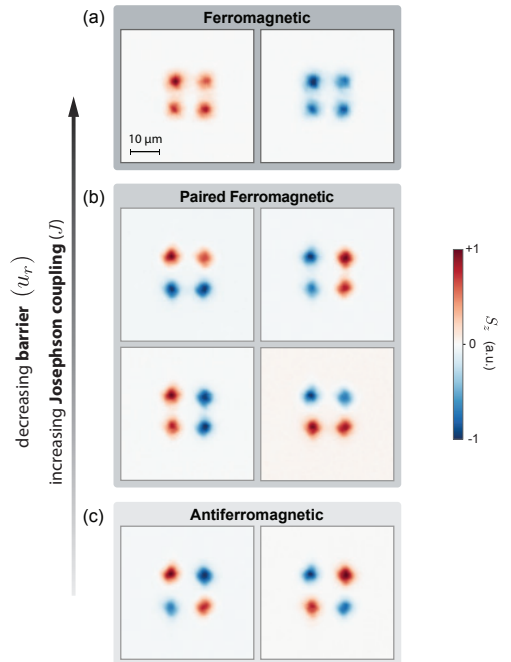


FIG. 2. Steady states as a function of barrier height. The measured condensate spin S_z for all possible stable states at three phases of (a) FM, (b) PFM, and (c) AFM, when the global NN barrier u_r is increased.

forms in the spin-up or spin-down state with a degree of circular polarization (condensate spin) $|S_z| > 85\%$. Polariton condensates created by the excitation pattern shown in Fig. 1b form a closed chain because the potential from the central pump spot is so large that the tunneling of polaritons between diagonal sites is negligible. Therefore, only the nearest neighbor coupling is significant. In this geometry the spins of each condensate are on-site coherently coupled by ϵ , and each is coherently coupled to that of the neighboring condensate by J (Fig. 1d). By varying the power of the central pump spot (Fig. 1b) we tune J , and by changing the relative ratio of J/ϵ we can change the magnetic order of the chain. Remarkably, the condensate chains exhibit distinct magnetic phases and mostly align their spins into particular patterns depending on their coupling strengths. Initially we explore a 4-condensate system, before showing how this behavior develops in the 8-condensate version.

Magnetized condensation at the minima of the optically-induced lattice potential is seen in the real-space photoluminescence (PL) from below to above the condensation threshold (Fig. 1e). The critical magnetization threshold is 1.3 times the condensation threshold. We denote the intensity of the central pump spot relative to the rest of the lattice spots by u_r . Since the local blueshift generated by the pump is linearly proportional to the intensity of the pump spots, the barrier height between each neighboring condensate increases as u_r increases. Thus u_r is a measure of the coupling strength (Josephson tunneling rate J) of the condensate lattice

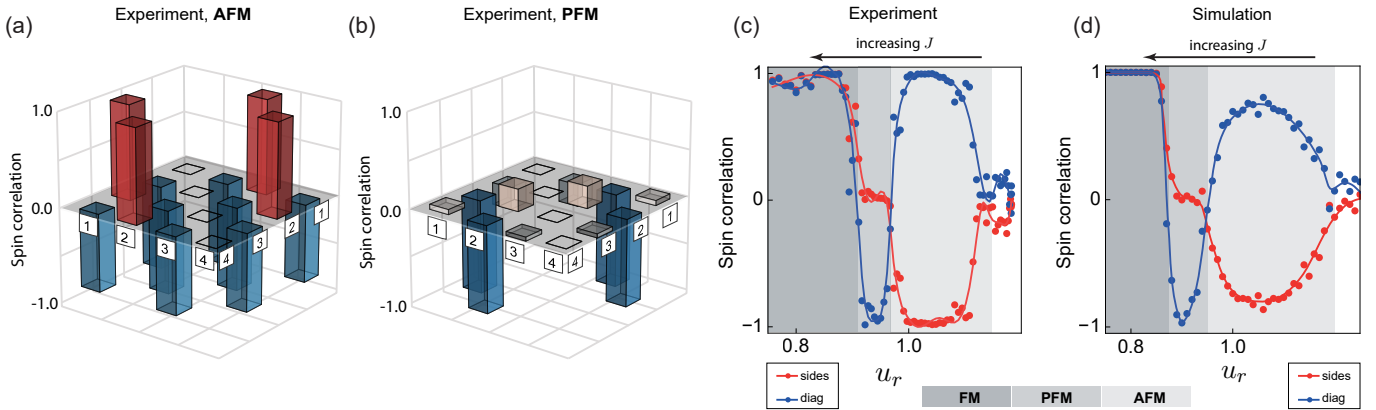


FIG. 3. Spin correlations as a function of barrier height. (a,b) The measured correlation matrix of the spin chain at the two phases of (a) AFM and (b) PFM. Numbers show condensate indices. The auto-correlated diagonal elements are removed for clarity. (c,d) Phase diagram of the spin chain showing spin correlation of the diagonal and side condensates vs u_r in (c) experiment and (d) 2D numerical simulations.

i.e. increasing u_r corresponds to decreasing J . Since each condensate can form in the spin-up or the spin-down states and couples with its two neighboring condensates, we expect to see the formation of different spin patterns around the chain as we tune u_r .

We observe four distinct phases of the spin chain as we increase u_r (Fig. 2): (1) FM with two spin degenerate states, formed from all spin-up or spin-down states, (2) paired ferromagnetic (PFM) separated by two domain walls, with four possible spin degenerate states and zero total spin, (3) AFM with two possible spin degenerate states, and (4) paramagnetism with nearly zero spin correlations between condensates (see also SI. 2). In each case, the spin chain spontaneously collapses into any of the degenerate states due to random spin fluctuations from the reservoir at the onset of magnetization. Although the final state of the chain is indeterminate for each realization, once the spin chain forms it stays in that particular steady state if a longer pump pulse (eg. 100 ms) is applied.

To characterize the spin correlations in each phase, we calculate the 4×4 correlation matrix C where the elements $C_{mn} = \rho(S_{z,m}, S_{z,n})$ are the Pearson correlation of spins of condensates m and n (as labelled in Fig. 1c,d). The correlation matrices for 100 realizations in the AFM and PFM regimes (Fig. 3a,b) demonstrate robustly correlated spin chains. To build their phase diagram we plot the average diagonal $\bar{C}_{\text{diag}} = (C_{13} + C_{24})/2$ and side $\bar{C}_{\text{side}} = (C_{12} + C_{23} + C_{34} + C_{41})/4$ condensate spin correlations as a function of u_r (Fig. 3c). We observe the FM phase for $u_r < 0.9$ followed by a sharp and narrow crossover to PFM for $0.9 < u_r < 0.96$ and a second sharp crossover to a broad AFM phase for $0.96 < u_r < 1.1$, succeeded by a rapid decay of correlations to near zero at higher u_r . 2D Ginzburg-Landau numerical simulations (see SI. 4) accurately reproduce the experimental phase map (Fig. 3d).

We can easily extend the square pumping geometry

to accommodate longer spin chains forming now a total of 8 condensates (Fig. 4a,b). Once again, we observe FM, AFM, and a variety of spin glass states in this magnetic chain. Because the number of barriers to modulate increases, their simultaneous control is not as straightforward. At the same time, as the system size increases, tiny spatial inhomogeneities in the microcavity become increasingly important. The latter arise from the growth process and slightly change the local energy of the polaritons, modulating the coupling strength between neighboring sites. If the energy modulation is large enough, it can even change the type of the coupling at each bond. Without more sophisticated approaches, this spatial inhomogeneity of the microcavity would limit the size of condensate lattices that can be studied, and thus prospects for using the system as a simulator. This general issue is however generic in all condensate lattices.

We can, however, explore and correct for the spatial inhomogeneity here by tailoring the imprinted excitation pattern. Since the background energy landscape is unknown, we employ an iterative search algorithm with feedback to find the optimal pattern needed to produce a desired correlated spin chain (see SI. 3). At the end of each search process, which only takes a few minutes, the most likely spin states can be inspected (Fig. 4c). Principal component analysis (PCA) of the spin-up and spin-down intensities reveals the most probable states after optimization (Fig. 4d). In the FM and AFM phases, the pure states (1st PCA components) are obtained in 60% of instances, more than twice as likely as trapping a single defect (2nd PCA component) with two domain walls. Other states have $< 10\%$ probabilities. By contrast, in the glass state we find near-degenerate states with four domain walls that dominate. Our 2-dimensional (2D) simulations show that a disorder potential of $\sim 5 \mu\text{eV}$ is enough to break spin chain symmetry (see SI. 4). We thus show this method can initialize the spin chain in any desired state.

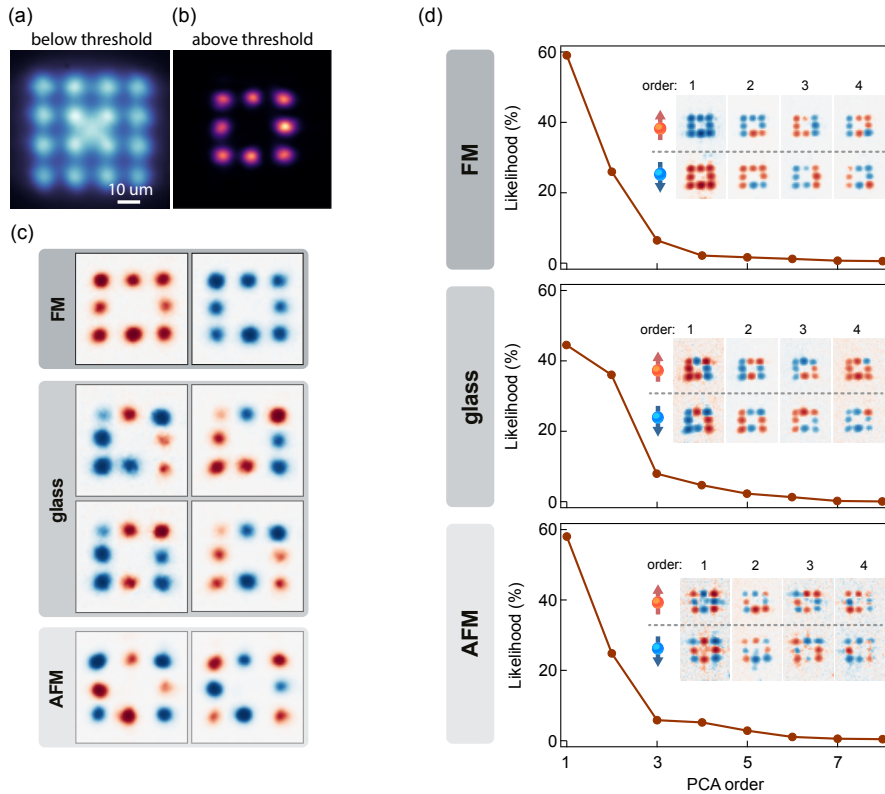


FIG. 4. Controlling magnetic order with feedback. (a) PL below threshold showing excitation pattern. (b) Emission above threshold showing 8-condensate chain. (c) The most probable spin states after optimization using FM, glass, or AFM search criteria in **d**. (d) PCA components of spin-up/down emission after the search procedure for different targets. Intensities show strengths of components. Plots show likelihood (variance percentage) for each order.

We outline here a mean-field theory, extended from single trapped condensates [22, 41] to include the Josephson coupling between nearest neighbors [23]. The order parameter for each exciton-polariton condensate is a two-component complex vector $\Psi_n = [\psi_{n+}, \psi_{n-}]^T$ where ψ_{n+} and ψ_{n-} are the spin-up and spin-down wave functions of condensate n . The order parameters evolve according to the driven dissipative equation:

$$\begin{aligned}
 i\dot{\Psi}_n = & -\frac{i}{2}g(S_n)\Psi_n - \frac{i}{2}(\gamma - i\epsilon)\sigma_x\Psi_n & (1) \\
 & + \frac{1}{2}(\bar{\alpha}S_n + \alpha S_{nz}\sigma_z)\Psi_n & (\text{interactions}) \\
 & - \frac{J}{2}(\Psi_{n-1} + \Psi_{n+1}). & (\text{Josephson coupling})
 \end{aligned}$$

Here, $g(S_n) = \Gamma - W + \eta S_n$ is the pumping-dissipation balance, Γ is the (average) dissipation rate, W is the incoherent in-scattering, $S_n = (|\psi_{n-}|^2 + |\psi_{n+}|^2)/2$ and η captures the gain-saturation term [42]. Linearly-polarized single-polariton states in X (horizontal) and Y (vertical) are split in energy by ϵ and in dissipation rate by γ , and $\sigma_{x,z}$ are the Pauli matrices. The non-linear interaction constants are given by $\bar{\alpha} = \alpha_1 + \alpha_2$ and $\alpha = \alpha_1 - \alpha_2$, where α_1 is the interaction constant for polaritons with the same spin and α_2 is the interaction constant for polaritons with opposite spins. Finally, $J > 0$ is the spin-

preserving Josephson coupling [43–45] between nearest-neighbor condensates.

By making an ansatz where FM (AFM) bonds have a relative phase of 0 (π) between nearest neighbors, we construct a mean-field model (see SI. 5). This maps the system to a single condensate with an energy shift ω_J and a renormalized polarization splitting ϵ_J . This allows us to apply the findings of ref. [22] for a single condensate to explain the phase-diagram of Fig. 3c,d, using two criteria: (1) the final state must be stable, and (2) if multiple states are stable, then the most probable final state is the one which turns magnetic at the lowest power. To be stable requires $\epsilon_J > 0$, so that on-site spin coupling is strong enough to give magnetized condensates. In addition, the spin-bifurcation threshold favors states with low ϵ_J (See Eq. S7). The three most favorable spin phases then yield modified splittings: $\epsilon_J^{\text{FM}} = \epsilon$, $\epsilon_J^{\text{glass}} = \epsilon - J$, $\epsilon_J^{\text{AFM}} = \epsilon - 2J$. Hence, the phase-diagram of Fig. 3c is explained as follows. For $J < \epsilon/2$, all three states are stable but the AFM state is favored since it has the lowest ϵ_J . For $\epsilon/2 < J < \epsilon$, the AFM state becomes unstable and the glass state is selected since it is now the lowest threshold state. For $J > \epsilon$, only the FM state is stable. This explains all the key behaviours observed.

In conclusion, we demonstrate control of the spin states

of closed chains of 4 and 8 polariton condensates. For small chains, the non-equilibrium driven-dissipative spin lattice gives rise to a unique paired spin (paired-FM) ordered state. This observation shows that our system is not governed by the minimization of free-energy, as in for example the standard equilibrium Ising model. To our knowledge, this paired-FM phase has not been observed in any equilibrium or non-equilibrium binary spin system. In a 2D square lattice, in the paired-FM phase each site must have two FM and two AFM bonds. Realizations of this phase can be mapped to different tilings of a chessboard with dominoes, which is a $\#P$ -complete problem [46]. We find that sample inhomogeneity hinders straightforward scaling to larger chains. We overcome this problem by careful feedback algorithms that com-

pensate for sample inhomogeneities and demonstrate a proof-of-principle scaling method. In the absence of any corrections, the system behaves like spin glass, where interactions are randomly chosen by the sample inhomogeneities acting as “quenched disorder”.

Acknowledgments—We acknowledge grants EPSRC EP/L027151/1, EU INDEX 289968, ERC “POLAFLOW” Starting grant, ERC LINASS 320503, Spanish MEC (MAT2008-01555), Mexican CONACYT 251808, EU FP7-REGPOT-2013-1 grant agreement 316165 II, Leverhulme Trust Grant No. VP1-2013-011 and Fundación La Caixa. H.S. and I.S. acknowledge support by the Research Fund of the University of Iceland, The Icelandic Research Fund, Grant No. 163082-051. TL was supported by the MOE AcRF Tier 1 grant 2016-T1-001-084.

-
- [1] R. J. Baxter, *Exactly Solved Models in Statistical Mechanics* (Elsevier, 1989).
- [2] S. Kirkpatrick, C. D. Gelatt, and M. P. Vecchi, *Science* **220**, 671 (1983).
- [3] A. Lucas, *Front. Physics* **2**, 5 (2014).
- [4] M. Hayashi, M. Yamaoka, C. Yoshimura, T. Okuyama, H. Aoki, and H. Mizuno, *Int. J. Net. Comp.* **6**, 195 (2016).
- [5] M. Yamaoka, C. Yoshimura, M. Hayashi, T. Okuyama, H. Aoki, and H. Mizuno, *Hitachi Rev.* **65**, 156 (2016).
- [6] F. Barahona, *J. Phys. A: Math. Gen.* **15**, 3241 (1982).
- [7] I. Buluta and F. Nori, *Science* **326**, 108 (2009).
- [8] I. M. Georgescu, S. Ashhab, and F. Nori, *Rev. Mod. Phys.* **86**, 153 (2014).
- [9] I. Bloch, J. Dalibard, and S. Nascimbène, *Nature Phys.* **8**, 267 (2012).
- [10] A. Marandi, Z. Wang, K. Takata, R. L. Byer, and Y. Yamamoto, *Nature Photon.* **8**, 937 (2014).
- [11] T. Inagaki, K. Inaba, R. Hamerly, K. Inoue, Y. Yamamoto, and H. Takesue, *Nature Photon.* **10**, 415 (2016).
- [12] I. Mahboob, H. Okamoto, and H. Yamaguchi, *Sci. Adv.* **2**, e1600236 (2016).
- [13] M. Taiji, N. Ito, and M. Suzuki, *Rev. Sci. Instrument.* **59**, 2483 (1988).
- [14] H. Deng, G. Weihs, C. Santori, J. Bloch, and Y. Yamamoto, *Science* **298**, 199 (2002).
- [15] J. Kasprzak, M. Richard, S. Kundermann, A. Baas, P. Jeambrun, J. M. J. Keeling, F. M. Marchetti, M. H. Szymańska, R. André, J. L. Staehli, *et al.*, *Nature* **443**, 409 (2006).
- [16] R. Balili, V. Hartwell, D. Snoke, L. Pfeiffer, and K. West, *Science* **316**, 1007 (2007).
- [17] J. Baumberg, A. Kavokin, S. Christopoulos, A. Grundy, R. Butté, G. Christmann, D. Solnyshkov, G. Malpuech, G. Baldassarri Höger von Högersthal, E. Feltin, *et al.*, *Phys. Rev. Lett.* **101**, 136409 (2008).
- [18] C. Schneider, A. Rahimi-Iman, N. Y. Kim, J. Fischer, I. G. Savenko, M. Amthor, M. Lermer, A. Wolf, L. Worschech, V. D. Kulakovskii, I. A. Shelykh, M. Kamp, S. Reitzenstein, A. Forchel, Y. Yamamoto, and S. Höfling, *Nature* **497**, 348 (2013).
- [19] P. Bhattacharya, B. Xiao, A. Das, S. Bhowmick, and J. Heo, *Phys. Rev. Lett.* **110**, 206403 (2013).
- [20] K. S. Daskalakis, S. A. Maier, R. Murray, and S. Kéna-Cohen, *Nat. Mater.* **13**, 271 (2014).
- [21] J. D. Plumhof, T. Stöferle, L. Mai, U. Scherf, and R. F. Mahrt, *Nat. Mater.* **13**, 247 (2014).
- [22] H. Ohadi, A. Dreismann, Y. G. Rubo, F. Pinsker, Y. del Valle-Inclan Redondo, S. I. Tsintzos, Z. Hatzopoulos, P. G. Savvidis, and J. J. Baumberg, *Phys. Rev. X* **5**, 031002 (2015).
- [23] H. Ohadi, Y. del Valle-Inclan Redondo, A. Dreismann, Y. G. Rubo, F. Pinsker, S. I. Tsintzos, Z. Hatzopoulos, P. G. Savvidis, and J. J. Baumberg, *Phys. Rev. Lett.* **116**, 106403 (2016).
- [24] A. V. Kavokin, J. Baumberg, G. Malpuech, and F. P. Laussy, *Microcavities* (Oxford Univ. Press, Oxford, 2007).
- [25] P. G. Savvidis, J. J. Baumberg, R. M. Stevenson, M. S. Skolnick, D. M. Whittaker, and J. S. Roberts, *Phys. Rev. Lett.* **84**, 1547 (2000).
- [26] C. Leyder, M. Romanelli, J. P. Karr, E. Giacobino, T. C. H. Liew, M. M. Glazov, A. V. Kavokin, G. Malpuech, and A. Bramati, *Nature Phys.* **3**, 628 (2007).
- [27] K. G. Lagoudakis, T. Ostatnický, A. V. Kavokin, Y. G. Rubo, R. André, and B. Deveaud-Plédran, *Science* **326**, 974 (2009).
- [28] T. K. Paraíso, M. Wouters, Y. Léger, F. Morier-Genoud, and B. Deveaud-Plédran, *Nat. Mater.* **9**, 655 (2010).
- [29] M. Abbarchi, A. Amo, V. G. Sala, D. D. Solnyshkov, H. Flayac, L. Ferrier, I. Sagnes, E. Galopin, A. Lemaître, G. Malpuech, and J. Bloch, *Nat. Phys.* **9**, 275 (2013).
- [30] P. Cristofolini, A. Dreismann, G. Christmann, G. Franchetti, N. G. Berloff, P. Tsotsis, Z. Hatzopoulos, P. G. Savvidis, and J. J. Baumberg, *Phys. Rev. Lett.* **110**, 186403 (2013).
- [31] V. G. Sala, D. D. Solnyshkov, I. Carusotto, T. Jacqmin, A. Lemaître, H. Terças, A. Nalitov, M. Abbarchi, E. Galopin, I. Sagnes, *et al.*, *Phys. Rev. X* **5**, 011034 (2015).
- [32] S. Dufferwiél, F. Li, E. Cancellieri, L. Giriunas, A. A. P. Trichet, D. M. Whittaker, P. M. Walker, F. Fras, E. Clarke, J. M. Smith, M. S. Skolnick, and D. N.

- Krizhanovskii, *Phys. Rev. Lett.* **115**, 246401 (2015).
- [33] A. Amo, T. C. H. Liew, C. Adrados, R. Houdre, E. Giacobino, A. V. Kavokin, and A. Bramati, *Nature Photon.* **4**, 361 (2010).
- [34] D. Ballarini, M. De Giorgi, E. Cancellieri, R. Houdré, E. Giacobino, R. Cingolani, A. Bramati, G. Gigli, and D. Sanvitto, *Nat. Commun.* **4**, 1778 (2013).
- [35] R. Cerna, Y. Léger, T. K. Paraíso, M. Wouters, F. Morier-Genoud, M. T. Portella-Oberli, and B. Deveaud, *Nat. Commun.* **4**, 2008 (2013).
- [36] H. S. Nguyen, D. Vishnevsky, C. Sturm, D. Tanese, D. Solnyshkov, E. Galopin, A. Lemaître, I. Sagnes, A. Amo, G. Malpuech, and J. Bloch, *Phys. Rev. Lett.* **110**, 236601 (2013).
- [37] A. Dreismann, H. Ohadi, Y. del Valle-Inclan Redondo, R. Balili, Y. G. Rubo, S. I. Tsintzos, G. Deligeorgis, Z. Hatzopoulos, P. G. Savvidis, and J. J. Baumberg, *Nat. Mater.* **15**, 1074 (2016).
- [38] E. Wertz, L. Ferrier, D. D. Solnyshkov, R. Johne, D. Sanvitto, A. Lemaître, I. Sagnes, R. Grousson, A. V. Kavokin, P. Senellart, G. Malpuech, and J. Bloch, *Nature Phys.* **6**, 860 (2010).
- [39] G. Tosi, G. Christmann, N. G. Berloff, P. Tsotsis, T. Gao, Z. Hatzopoulos, P. G. Savvidis, and J. J. Baumberg, *Nature Phys.* **8**, 190 (2012).
- [40] A. Askitopoulos, H. Ohadi, A. V. Kavokin, Z. Hatzopoulos, P. G. Savvidis, and P. G. Lagoudakis, *Phys. Rev. B* **88**, 041308 (2013).
- [41] I. L. Aleiner, B. L. Altshuler, and Y. G. Rubo, *Phys. Rev. B* **85**, 121301 (2012).
- [42] J. Keeling and N. G. Berloff, *Phys. Rev. Lett.* **100**, 250401 (2008).
- [43] K. G. Lagoudakis, B. Pietka, M. Wouters, R. André, and B. Deveaud-Plédran, *Phys. Rev. Lett.* **105**, 120403 (2010).
- [44] M. Wouters, *Physical Review B* **77**, 121302 (2008).
- [45] M. O. Borgh, J. Keeling, and N. G. Berloff, *Physical Review B* **81**, 235302 (2010).
- [46] J. Matousek, *Thirty-three Miniatures: Mathematical and Algorithmic Applications of Linear Algebra* (American Mathematical Society, Providence, R.I., 2010) Chap. 22.
- [47] P. Tsotsis, P. S. Eldridge, T. Gao, S. I. Tsintzos, Z. Hatzopoulos, and P. G. Savvidis, *N. J. Phys.* **14**, 023060 (2012).
- [48] M. Wouters and I. Carusotto, *Phys. Rev. Lett.* **99**, 140402 (2007).
- [49] M. Wouters, T. C. H. Liew, and V. Savona, *Phys. Rev. B* **82**, 245315 (2010).

Supplemental Information

1. SAMPLE AND EXPERIMENTAL TECHNIQUES

The cavity top (bottom) distributed Bragg reflector (DBR) is made of 32 (35) pairs of $\text{Al}_{0.15}\text{Ga}_{0.85}\text{As}/\text{AlAs}$ layers of 57.2 nm/65.4 nm. Four sets of three 10 nm GaAs quantum wells (QW) separated by 10 nm thick layers of $\text{Al}_{0.3}\text{Ga}_{0.7}\text{As}$ are placed at the maxima of the cavity light field. The $5\lambda/2$ (583 nm) cavity is made of $\text{Al}_{0.3}\text{Ga}_{0.7}\text{As}$. The sample shows condensation under non-resonant excitation [47].

The quasi continuous wave pump is a single-mode Ti:Sapphire laser tuned to the first Bragg mode ~ 100 meV above the condensate energy, and is linearly polarized. In order to drive condensate formation on short time scales, the pump is amplitude-modulated by an acousto-optic modulator. A spatial light modulator (SLM) is used to spatially pattern the pump beam into a square lattice. A 0.4 NA objective is used for imaging the pattern onto the sample. A cooled CCD and a 0.55 m spectrometer is used for imaging and energy resolving the emission. Polarization is analysed using a quarter-waveplate and a Wollaston prism in front of the camera. The CCD and the pump laser are electronically synchronized. For each realization of the experiment, the sample is exposed to microsecond-long pump pulses, and the final spin state is measured. Many realizations are measured to build statistics.

2. MOMENTUM, REAL-SPACE AND POTENTIAL LANDSCAPE

Fig. S1a shows the logarithmic scale of the momentum space intensity at below condensation threshold. The cavity detuning here is -2 meV to -3 meV. As the pumping power increases we observe a continuous blueshift of up to ~ 300 μeV until the condensates reach the spin bifurcation threshold. At this threshold, all 4 lattice sites condense to the ground state of the dispersion at a single energy to within the resolution of our spectrometer (Fig. S1b). Fig. S1c shows the potential landscape. At the pump spots the blueshift is ~ 600 μeV at $u_r = 1$, whereas at the saddle points it drops to ~ 300 μeV . The confining potential at the saddle points is ~ 80 μeV .

Fig. S2 shows the σ_+ and σ_- polarized intensity of the condensate chain stable states at FM, PFM and AFM regimes. The minimum circular polarization of the condensates is 75%.

3. FEEDBACK SEARCH

The search algorithm starts with equal intensities across the array and randomly changes each pump spot intensity by up to of 10% on each step. For each iteration we record 100 realizations and calculate the average NN spin correlation \bar{C}_{NN} as a figure of merit. To seek an AFM chain, we look for configurations where \bar{C}_{NN} is minimized, retaining intensity patterns that result in a smaller \bar{C}_{NN} . A typical example of this iterative process is shown in Fig. S3a. With 1 s per iteration the search time for desired spin chains is only minutes. For FM chains \bar{C}_{NN} is instead maximized, while for the glass state $|\bar{C}_{NN}|$ is minimized (Fig. S3b).

In principle, the correction mechanism is scalable to larger lattices, and only needs to be applied once. The limiting factors are in fact the total pump intensity and the field of view of the objective. The efficiency of our optical setup is currently 20%, meaning that for 1W

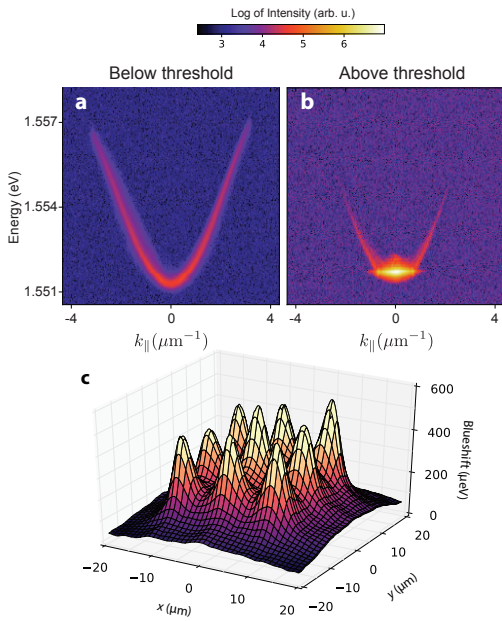


FIG. S1. Momentum and potential landscape. (a) In-plane energy-resolved momentum below threshold in-plane momentum, and (b) above threshold. (c) The pump-induced potential.

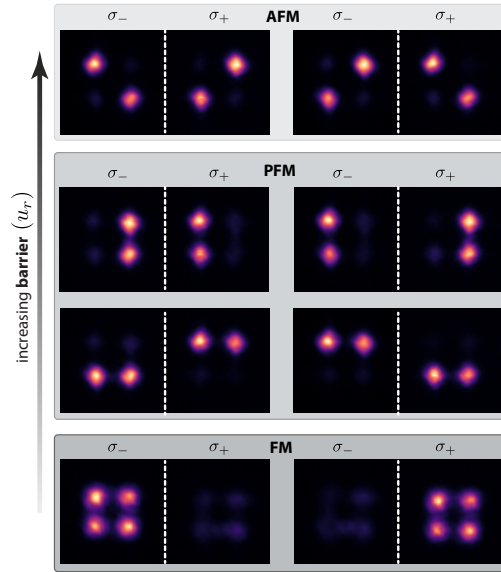


FIG. S2. Real-space polarization-resolved intensity. Spin-up (σ_+) and spin-down (σ_-) intensities of steady states as barrier is increased.

pump laser we get 200 mW patterned power on the sample. For condensation we require ~ 5 mW per spot (4 spots for a site), which is currently limiting us to a 8×8 -condensate lattice (2 W pump laser). The other limiting factor is the field of view of the objective. Currently each site is $\sim 10 \mu\text{m}$ and in order to get the required pump spot resolution of $\sim 1 \mu\text{m}$, we need to work with high numerical aperture objectives, which limit our field of view to ~ 1 mm diameters, effectively limiting us to 100×100 -condensate lattices, but large enough to study intriguing experiments.

4. MONTE-CARLO SIMULATIONS

A. zero-dimensional

We perform Monte-Carlo simulations while J is varied. We perform 2000 realizations that lasts 4 ns with random initial conditions for each J and calculate the correlations of the final state s_z of the condensate realizations. Fig. S10 shows the correlation of the sides and diagonal condensates versus the Josephson coupling strength J at $P = 1.1P_c$. We observe a qualitatively similar behavior as the 2D simulations: as J reduces we go from FM to PFM to AFM phases. The parameters used for 0D simulations were $W = 0.2 \text{ ps}^{-1}$; $\Gamma = 0.1 \text{ ps}^{-1}$; $\epsilon = 0.04 \text{ ps}^{-1}$; $\gamma = 0.2\epsilon$; $\alpha_1 = 0.01 \text{ ps}^{-1}$; $\alpha_2 = -0.5\alpha_1$; $\eta = 0.02 \text{ ps}^{-1}$.

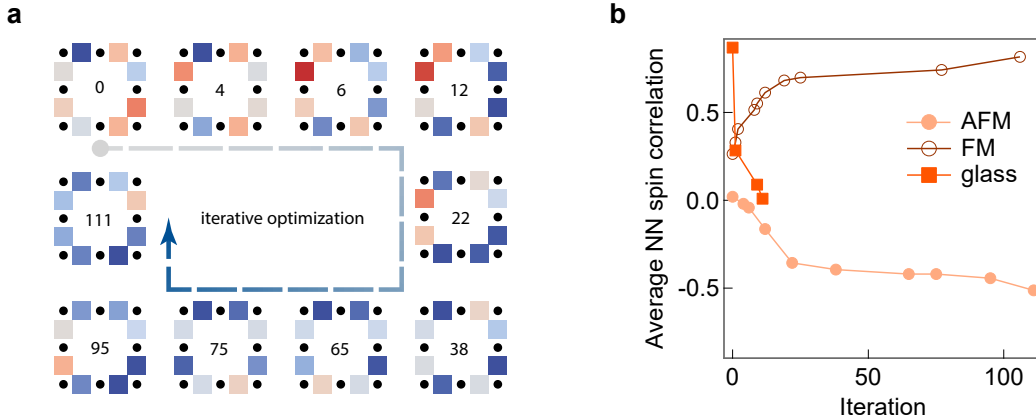


FIG. S3. Feedback search (a) Example of iterative search for AFM spin chain, showing the spin correlation of the bonds (indices show iteration number). Blue links denote AFM bonds and reds are FM bonds and colour scales are as in Fig. 2. Indexes show the iteration number. (b) Average nearest-neighbor spin correlation as a function of search iteration step for three search criteria of FM, glass and AFM target phases.

B. 2-dimensional

For 2D simulations we use a complex Ginzburg-Landau-type equation [42, 48] based on equation 1, which in addition incorporates the Laplacian, a repulsive potential due to the excitons in the pump spots, and energy relaxation [49] for polaritons in the trap:

$$i\dot{\Psi} = -\frac{i}{2}[g(S) - \gamma\sigma_x]\Psi + (1 - i\Lambda)\left[\frac{1}{2}[(\alpha_1 + \alpha_2)S + (\alpha_1 - \alpha_2)S_z\sigma_z]\Psi - \frac{1}{2}\epsilon\sigma_x\Psi - \frac{\nabla^2}{2m^*}\Psi + (V_p + V_s)\Psi\right]. \quad (\text{S1})$$

Here, m^* is the effective mass of the polaritons and the harvest rate is given by $W = rP/\Gamma_R$, where P is the spin-independent spatial profile of the excitation, Γ_R is the decay rate of the exciton reservoir, and r is the incoming rate of polaritons into the condensate. The gain saturation is given by $\eta = r^2P/\Gamma_R^2$, and it depends on the total occupation of the condensate (more generally treated in ref. 22). The repulsive potential due to the interaction of polaritons with the exciton reservoir is given by $V_p = \frac{1}{2}g_rN + \frac{1}{2}g_P P$, where g_r and g_P are the interaction constants of polaritons with the exciton reservoir and the pump spot respectively ($\hbar = 1$), and $N = g(S)/r$ is the density of the exciton reservoir. Background potential due to inhomogeneity in the sample is given by V_s . Finally, $\Lambda \ll 1$ is a phenomenological constant that accounts for the energy relaxation, and it is proportional to the pump intensity.

We initialize the coherent macroscopic wavefunction Ψ with random noise and evolve it until the steady state is achieved. We repeat this process for 150 realizations and map out the correlation matrix of the condensate at each u_r .

Fig. S4 shows typical realizations at three distinct regimes of AFM, glass and FM. For longer 8-condensate chains in the presence of a random background potential V_s , we observe the explicit appearance of glassy states as shown in Fig. S5. The random potentials in 2D simulations were acquired by adding randomly located Gaussian spots

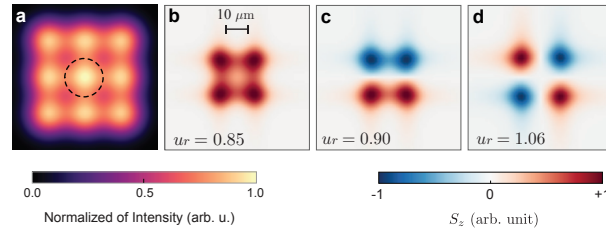


FIG. S4. Steady states 2D simulations. (a) Pump intensity pattern at $u_r = 1.08$. The variable pump spot intensity is marked by a dashed circle. (b-d) Condensate spin S_z for dominant states at (B) $u_r = 0.85$ (FM), (C) $u_r = 0.90$ (PFM) and (D) $u_r = 1.06$ (AFM).

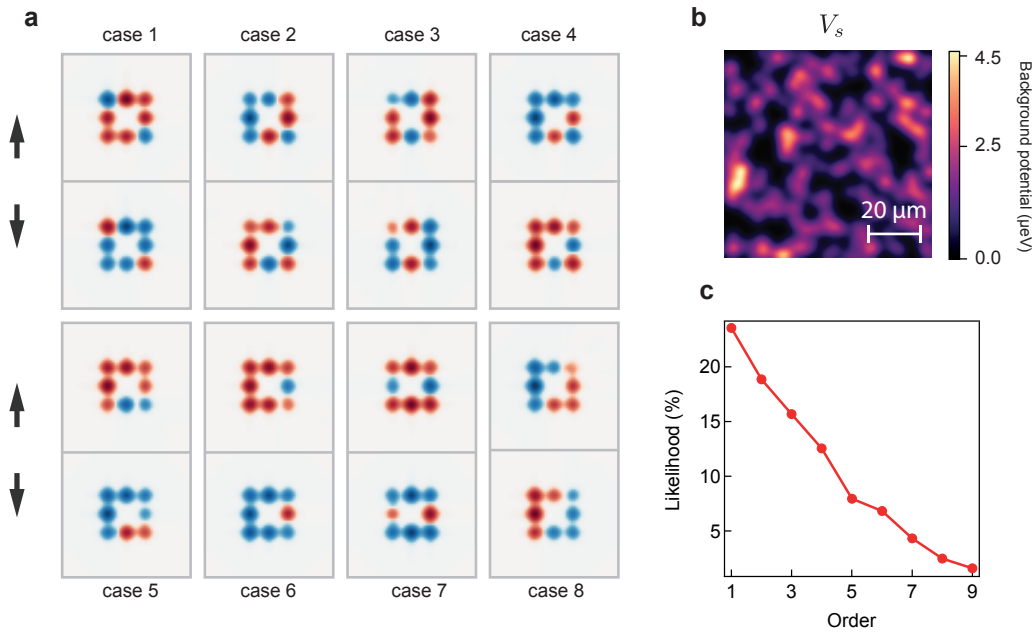


FIG. S5. 2D Simulations with random background potential (a) spin states at various cases of random background potential V_s . (b) Typical case of a random background potential. (c) Likelihood percentage of PCA orders for case 4.

with $1/e$ diameters of $12 \mu\text{m}$ and amplitudes of $0.8g_P$. Our 2D simulations show that a disorder potential of $\sim 5 \mu\text{eV}$ is enough to break spin chain symmetry.

The stronger correlation in the experiment compared to simulations in Fig. 3(c,d) is due to the ramp-time of the pump laser. In the experiments, the rise-time is about 50 ns. In the model, the turn-on is instantaneous. The slow rise-time effectively drives the condensates adiabatically into the state with the lowest threshold state resulting in a highly deterministic outcome for each realization of the experiment. By contrast, if the pump turns on much faster than the dynamics of the condensate, the system can overshoot the lowest magnetization threshold, resulting in a more probabilistic outcome for each realization. In the simulations, the pump laser is turned on instantaneously at the start of the simulation and we find the steady state after 2 ns. These simulations are

2D and each point is the average of 150 realizations and calculating the whole graph takes about a day. In principle, one can incorporate the slow rise-time of the pump, but at the moment simulating adiabatic pumping unfortunately is beyond our current computational capacity.

The parameters used in the 2D simulations are $\hbar\alpha_1 = 2 \mu\text{eV}\mu\text{m}^2$; $\alpha_2 = -0.5\alpha_1$; $\hbar g_r = 23 \mu\text{eV}\mu\text{m}^2$; $g_P = g_R/4$; $\Lambda = 0.1$; $m^* = 5.1 \times 10^{-5}m_e$; $r = 0.05 \text{ps}^{-1}\mu\text{m}^2$; $\Gamma_R = 10 \text{ps}^{-1}\mu\text{m}^2$; $\Gamma = 0.2 \text{ps}^{-1}\mu\text{m}^2$; $\hbar\epsilon = 10 \mu\text{eV}$; $\gamma = 0.5\epsilon$.

5. QUALITATIVE ANALYSIS OF STEADY SPIN STATES

A. Mean-field model

The rate equations have a symmetry that can map the system onto a single condensate, using the ansatz:

$$\begin{aligned}\Psi_{n+1} &= e^{i\varphi_{n+1,n}}\Psi_n, & (\text{FM bond}) \\ \Psi_{n+1} &= e^{i\varphi_{n+1,n}}\sigma_x\Psi_n, & (\text{AFM bond})\end{aligned}\tag{S2}$$

where the phase-factors of each bond are to be determined. Making this ansatz, Eq. 1 can be written as:

$$\begin{aligned}i\dot{\Psi}_n &= -\frac{i}{2}(g(S_n) + i\omega_J)\Psi_n - \frac{i}{2}(\gamma - i\epsilon_J)\sigma_x\Psi_n \\ &+ \frac{1}{2}(\bar{\alpha}S_n + \alpha S_{nz}\sigma_z)\Psi_n.\end{aligned}\tag{S3}$$

This corresponds to a single condensate with a renormalized effective in-plane B-field ϵ_J , arising from AFM bonds, and an energy-shift ω_J arising from the FM bonds. The strength of these parameters depends on the relative phases between nearest neighbors in the system. For condensate n one can write

$$\begin{aligned}\epsilon_J &= \epsilon + J(\delta_{nk}e^{i\varphi_{nk}} + \delta_{nl}e^{i\varphi_{nl}}) \\ \omega_J &= -J((1 - \delta_{nk})e^{i\varphi_{nk}} + (1 - \delta_{nl})e^{i\varphi_{nl}}),\end{aligned}\tag{S4}$$

where k, l are the nearest neighbors and $\delta_{nm} = 1, 0$ for AFM or FM bonding respectively. Here φ_{nm} is the phase shift moving from condensate n to m . By mapping the system to a single mean-field condensate, we can take advantage of the single condensate analysis given in ref. 22, in particular the magnetization threshold $S_c = (\epsilon_J^2 + \gamma^2)/\alpha\epsilon_J$, which for $\gamma < \epsilon$ is minimized when ϵ_J is minimized.

B. Criteria for state to dominate

1. **The final state must be stable.** For a mean-field model, magnetization requires that $\epsilon_J > 0$ (see ref. 22).
2. **If multiple final states are stable, the state with the lowest spin bifurcation threshold is favored.** Following turn-on of the pump, the polariton number will increase, and the state that first reaches the polariton number spin-bifurcation

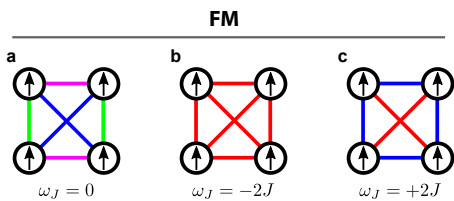


FIG. S6. Schematic showing the three possible FM solutions. Red lines show in-phase condensates ($\varphi_{nm} = 0$) whereas blue lines are anti-phase ($\varphi_{nm} = \pi$). The pink and green lines depict the arbitrary choice of phase between the nearest neighbors as long as the condensates diagonally across are anti-phase.

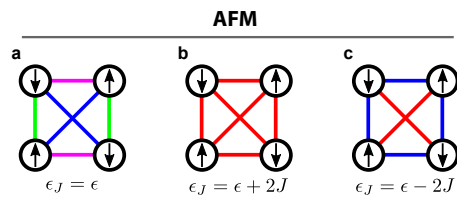


FIG. S7. Schematic showing the three possible AFM solutions. Red lines show in-phase condensates ($\varphi_{nm} = 0$) whereas blue lines are anti-phase ($\varphi_{nm} = \pi$). The pink and green lines depict the arbitrary choice of phase between the nearest neighbors as long as the condensates diagonally across are anti-phase.

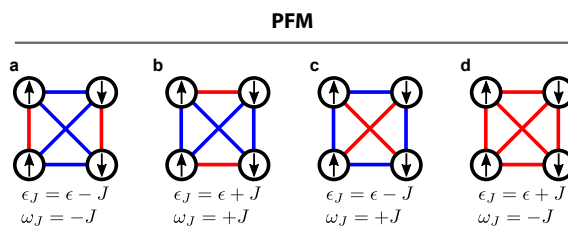


FIG. S8. Schematic showing the four possible PFM solutions. Blue lines are anti-phase condensates ($\varphi_{nm} = \pi$) and red are in-phase ($\varphi_{nm} = 0$).

threshold is the most probable final state. For a mean-field model, the critical spin-bifurcation threshold is given by Eq. (4) of ref. 22:

$$S_c = \frac{\epsilon_J^2 + \gamma^2}{\alpha \epsilon_J}. \quad (\text{S5})$$

Hence, the system favors states with the lowest ϵ_J .

C. Application to 4 condensate system: stationary points

To identify the stationary points of the system, we can use the Mean-field model. We assume the stationary points are such that all condensates have equal total polariton populations (S_n). This requires that both ϵ_J and ω_J are real to avoid transferring population between condensate sites, and are same for all sites. In principle, one can have solutions where the magnitude of the spin is different for different sites, but these solutions are highly nontrivial and are out of the scope of the current work.

1. FM stationary points

For the FM state, since there are no AFM bonds, $\epsilon_J = \epsilon$. There are three possible ways to make $\omega_J = -J(e^{i\varphi_{nk}} + e^{i\varphi_{nl}})$ real and constant across all sites to have all 4 condensates phase locked:

1. The diagonal states are in anti-phase, $\omega_J = 0$ (Fig. S6a).

2. Nearest neighbors are in-phase, $\omega_J = -2J$ (Fig. S6b)
3. Nearest neighbors are anti-phase, $\omega_J = +2J$ (Fig. S6c)

Since all states have the same ϵ_J , they share the same spin-bifurcation threshold.

2. AFM stationary points

For the AFM state, since there are no FM bonds, $\omega_J = 0$. Similar to the FM state, there are three possible ways to make $\epsilon_J = -J(e^{i\varphi_{nk}} + e^{i\varphi_{nl}})$ real, and constant across all sites:

1. Sites diagonally across are anti-phase, $\epsilon_J = \epsilon$ is unchanged (Fig. S7a).
2. All nearest neighbors are in-phase, $\epsilon_J = \epsilon + 2J$ (Fig. S7b).
3. All nearest neighbors are anti-phase, $\epsilon_J = \epsilon - 2J$ (Fig. S7c).

By inspection of Eq. S5, AFM state (3) with anti-phase nearest neighbors has the smallest ϵ_J , and consequently the lowest spin bifurcation threshold of the possible AFM states.

3. PFM stationary points

For the PFM state, the system is characterized by each condensate having one FM bond and AFM bond. There are four possible combinations which are given in Fig. S8 which allow ω_J and ϵ_J to stay real. From the analysis above, one can easily see that the solutions are combinations of $\epsilon_J = \epsilon \pm J$ and $\omega_J = \pm J$ depending on whether the bonds are anti-phase or in-phase. The minimum bifurcation threshold then selects the state with an anti-phase AFM bond, such that $\epsilon_J = \epsilon - J$.

D. Mean-field phase diagram

The spin-bifurcation thresholds can be summarized as follows: $\epsilon_J > 0$ for the solution to exist but the smallest ϵ_J has the lowest threshold (see Eq. S5). Considering thus only solutions where ϵ_J is minimal, the coupling parameter J defines a boundary between AFM, PFM, and FM solutions which have two, one, and zero (anti-phase) AFM bonds respectively:

$$\begin{aligned}
 \epsilon_{FM} &= \epsilon, \\
 \epsilon_{PFM} &= \epsilon - J, \\
 \epsilon_{AFM} &= \epsilon - 2J.
 \end{aligned}
 \tag{S6}$$

Hence, for $J < \epsilon/2$, all spin states are stable, and the AFM state is observed since it has the lowest spin-bifurcation threshold. For $\epsilon/2 < J < \epsilon$, the AFM state is no longer stable, and the PFM state is observed since it has the lowest threshold. For $J > \epsilon$, only the FM states are stable, as shown in Fig. S9.

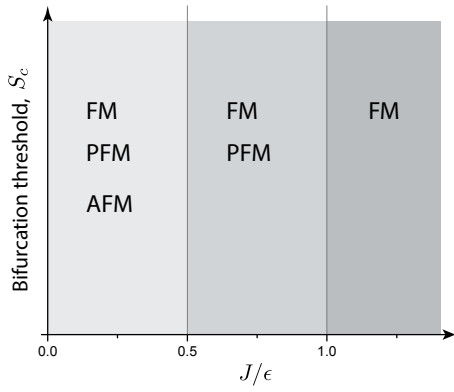


FIG. S9. Phase-diagram of 4 condensate system using a mean-field model. For small $J/\epsilon < 0.5$, all states are potentially stable. However the AFM state wins because it has the lowest spin bifurcation threshold. The AFM state becomes unstable for $J/\epsilon > 0.5$, and the PFM state is observed because it is now the state with the lowest threshold. For $J/\epsilon > 1$, only the FM state is stable.

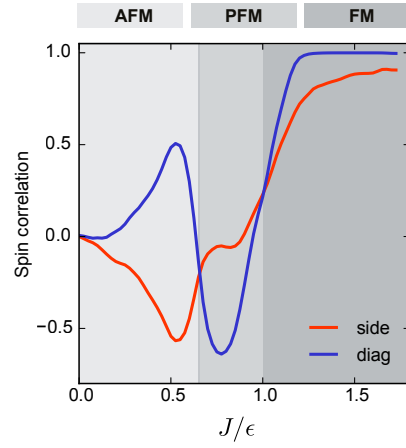


FIG. S10. 0D simulations Monte-Carlo simulations of the 0D model showing spin correlation of the side and diagonal condensates in a 4-condensate chain as a function of J/ϵ .